Phase-Field Lattice Boltzmann Study of Convection Effects on Dendritic Growth in Thin-Walled Al–0.576 wt% Cu Alloy

Jia-tuo An1, *Da-fan Du1, *Li-jun Zhang2, *An-ping Dong1 and Bao-de Sun1

- Shanghai Key Lab of Advanced High-temperature Materials and Precision Forming and State Key Lab of Metal Matrix Composites,
 School of Materials Science and Engineering, Shanghai Jiao Tong University, Shanghai, 200240, China
 - 2. State Key Laboratory of Powder Metallurgy, Central South University, Changsha, 410083, China

*Corresponding address: e-mail: dafand@sjtu.edu.cn

Abstract: Thin-walled castings are widely used in various industrial fields, but their micro-mechanism still requires in-depth research. To deeply study the micro-mechanism of dendrite growth in thin-walled spaces during casting, the phase-field lattice Boltzmann simulations of Al-0.576 wt% Cu alloy were performed to investigate the growth morphologies of equiaxed dendrites and directionally grown dendrites in thin-walled spaces under different convection states. The results show that solute plumes were generated in equiaxed dendrites under different convection conditions, and the primary dendrites upstream were more developed than those downstream. When $P_y = 0.01 \text{ m/s}^2$, the asymmetry degree of primary dendrites upstream and downstream decreased, and the inclination angles of primary dendrites on the left and right sides also decreased. Meanwhile, during the growth process of directionally grown dendrites, the convection form in the thin-walled space gradually changed from the coexistence state of natural convection and forced convection to the state dominated by natural convection. This paper reveals the micro-mechanism of dendrite growth in thin-walled spaces, which is helpful in providing theoretical guidance for actual production practice.

Keywords: phase-field method; solidification; dendritic growth

1 Introduction

As industries advance, the demand for lightweighting has been steadily increasing in various industry sectors, particularly within the aerospace industry. Accordingly, thin-walled structures have become widely used in many aerospace components, such as the aerospace engines [1]. However, traditional gravity casting (GC) techniques often lead to defects such as incomplete filling, inclusions, shrinkage porosity/cavities within thin-walled castings [1]. These conventional methods face even greater difficulties in producing high quality, complex-shaped thin-walled castings.

In recent years, the emergence and development of counter gravity casting (CGC) technology has offered a novel solution for manufacturing thin-walled components ^[2]. This technology has found widespread application in various industry sectors, including aerospace ^[1], automotive manufacturing ^[3, 4] and electronics ^[5]. Nowadays, the primary categories of CGC techniques include low pressure casting (LPC) ^[6], counter pressure casting (CPC) ^[7], vacuum suction

casting (VSC) ^[8], and adjusted pressure casting (APC) ^[9]. Different from GC, the CGC process involves the molten metal being subjected to an artificially applied force in the direction opposite to gravity, in addition to the gravitational force. As a result, in the CGC process, the filling speed of the melt is more stable and controllable, resulting in higher quality castings with virtually no inclusions such as oxides, or shrinkage porosity and cavities.

Experimental research has indicated that the applied pressure could influence the filling process and solidification process, leading to the fine and dense solidification microstructure, then the improvement of mechanical properties. Yan et al. [10] found that the increasing solidification pressure could enhance the extrusion and infiltration among the dendrites, making the solidification microstructure finer and denser. Li et al. [11] conducted real-time X-ray observations of the solidification process of Al-20 wt% Cu alloy under gravity in thin-walled spaces. They discovered that the filling and solidification behavior of the alloy melt

primarily depended on the wall thickness. As the wall thickness decreased, the dendritic network became denser, and the melt filling time was reduced. Simultaneously, dendrites nucleated on the colder wall surfaces and grew towards the center. Due to the confined space within thin-walled castings, convection between growing dendrites and the melt becomes significant during solidification. Therefore, the process of dendritic growth involves complex interactions among the flow field, solute field, temperature field, and solid-liquid phase transformation. Study of the individual parameters involved in such interactive process using traditional experimental methods is challenging. Currently, few research has investigated the microscopic mechanisms of dendritic growth under convection in confined thin-walled space. Therefore, simulation employing numerical methods investigate the multi-physics fields involved in these interactive processes is particularly crucial.

recent years, with the refinement and development of the phase-field method (PFM) and the lattice Boltzmann method (LBM), more and more researchers have adopted a coupled approach combining these two methods to simulate the process of dendritic growth. Zhang et al. [12] coupled the phase-field method with the Lattice Boltzmann Method to simulate the morphological evolution of equiaxed grains and dendrites in Al-4 wt% Cu alloy under both natural and forced convection. Their findings indicated that convection leads to the deflection of the dendritic primary trunk. Zhang et al. [13] simulated the directional solidification process of CM247LC alloy using a coupled phase-field and Lattice Boltzmann method, finding that the crystal orientation angle had a minor effect on the solute plume.

In this work, the PFM coupled with the multi-relaxation times (MRT) LBM D2Q9 model is utilized to investigate the impact of varying convection conditions on dendritic growth within thin-walled castings during solidification. From the perspective of microscopic mechanisms, we elucidate the characteristics of dendritic growth in thin-walled spaces under different convection conditions by fully

studying the dendritic morphologies, concentration distribution, and convection velocity distribution at the growth front of dendrites. This research aims to provide a theoretical basis for practical production.

2 Numerical methods

2.1 Phase-field model

The phase field model proposed by Karma et al. [14] for binary alloy was employed to simulate the evolution of phase field and concentration field. The governing equation of phase field can be described as below

$$\tau(\mathbf{n})^{2} \frac{\partial \phi}{\partial t} = \nabla \cdot \left[a_{s}(\mathbf{n})^{2} \nabla \phi \right] + \partial_{x} \left(|\nabla \phi|^{2} \ a_{s}(\mathbf{n}) \frac{\partial a_{s}(\mathbf{n})}{\partial \left(\partial_{x} \phi\right)} \right) + \partial_{y} \left(|\nabla \phi|^{2} \ a_{s}(\mathbf{n}) \frac{\partial a_{s}(\mathbf{n})}{\partial \left(\partial_{y} \phi\right)} \right) + \phi - \phi^{3} - \lambda \left(1 - \phi^{2} \right)^{2} \left(U + \theta \right)$$

$$(2.1)$$

in which ϕ is phase field variable, $\phi = 1$ represents solid phase, and $\phi = -1$ represents liquid phase. $\tau(n)$ is the relaxation time. For isothermal solidification,

$$\tau(\mathbf{n}) = \left[Mc_{\infty} \left(1 + \left(1 - k \right) U \right) \right] a_{s}(\mathbf{n})^{2}$$
 (2.2)

in which $M = |m|(1-k)/\Delta T_0$ is the dimensionless liquidus slope. m is the liquidus slope. k is the partition coefficient. $\Delta T_0 = |m|c_l^0(1-k)$ is the equilibrium solidification temperature range. c_l^0 is the equilibrium liquid composition at initial temperature T_0 . $a_s(n)$ is the anisotropy function, which can be expressed as

$$a_s(\mathbf{n}) = 1 - 3\varepsilon_4 + 4\varepsilon_4 \left(\phi_x^4 + \phi_y^4\right) / \left(\phi_x^2 + \phi_y^2\right)^2$$
 (2.3)

in which ε_4 is the anisotropic strength. $\lambda = a_1 W_0 / d_0$ is the coupling factor. $a_1 = 0.8839$ [15] is a constant, and W_0 is the solid-liquid interface width. $d_0 = \Gamma / \Delta T_0$ is the chemical capillary length. Γ is the Gibbs-Thomson coefficient. U is the dimensionless solute concentration, which can be described as

$$U = \frac{1}{1 - k} \left(\frac{2c / c_{\infty}}{1 + k - (1 - k)g(\phi)} - 1 \right)$$
 (2.4)

in which c is the solute concentration. c_{∞} is the nominal composition of alloy. $g(\phi) = \phi$ is the interpolation function. $\theta = (T - T_0)/\Delta T_0$ is the equivalent dimensionless undercooling, and T is the

temperature. For directional solidification, $\tau(n)$ can be temperature dependent, which can be expressed as

$$\tau(\mathbf{n}) = \left[1 - (1 - k)(G_x \cdot x - R \cdot t) / \Delta T_0\right] a_s(\mathbf{n})^2 \qquad (2.5)$$

in which G_x is the temperature gradient along X-direction, and x is the distance from the nucleation site. For directional solidification, the frozen temperature approximation was employed and can be described as

$$T = T_0 + G_x x - R \times t \tag{2.6}$$

in which R is the cooling rate, and t is the simulation time.

The governing equation for the evolution of concentration field can be described as

$$\left(\frac{1+k_{i}}{2} - \frac{1-k_{i}}{2}\phi\right)\frac{\partial U}{\partial t} = \nabla \cdot \left(\tilde{D}q(\phi)\nabla U + a(\phi)\left(1+\frac{1-k}{2}\right)U\right)\frac{\partial \phi}{\partial t}\frac{\nabla \phi}{|\nabla \phi|}\right) + \frac{1}{2}\left[1+\left(1-k\right)U\right]\frac{\partial \phi}{\partial t} - \frac{1}{2}\tilde{v}_{p} \cdot \left\{\left[1+k-\left(1-k\right)\phi\right]\nabla U - \left[1+\left(1-k\right)U\right]\nabla\phi\right\}\right]$$
(2.7)

in which $\tilde{D}=a_2\lambda$ is the dimensionless solutal diffusion coefficient in liquid phase. $a_2=0.6267$ [15] is a constant. $q(\phi)=\phi$ and $a(\phi)=\sqrt{2}/2$ are the interpolation functions. $\tilde{\boldsymbol{v}}_p$ is the dimensionless melt velocity, which can be expressed as

$$\tilde{\mathbf{v}}_p = a_1 a_2 \frac{\mathbf{v} d_0}{D} \left(\frac{W_0}{d_0} \right)^2 \tag{2.8}$$

in which D is the solute diffusion coefficient in liquid phase. v is the melt velocity.

2.2 MRT-LBM D2Q9 model

To model the melt flow behavior and convection, the MRT-LBM D2Q9 model [16] was employed in this work. The governing equation of particle distribution function (PDF) can be described as

$$f_{i}(\mathbf{x} + \mathbf{e}_{i}\delta x, t + \delta_{t}) = f_{i}(\mathbf{x}, t) - \Omega_{ij} \left[f_{j}(\mathbf{x}, t) - f_{j}^{eq}(\mathbf{x}, t) \right] + \delta t F_{i}(\mathbf{x}, t)$$

$$(2.9)$$

in which $f_i(x,t)$ and $f_i(x,t)$ are the PDFs at position x and time t along the ith and jth direction, respectively. $f_i^{eq}(x,t)$ is the equilibrium PDF at position x and time t along the jth direction position.

vector in the lattice space. δx is the space interval, and δ_t is the time interval. \mathbf{e}_i is the unit discrete velocity, which is expressed as

$$e_{i} = \begin{cases} (0,0), & i = 0\\ (\cos[(i-1)\pi/2], \sin[(i-1)\pi/2]), & i = 1-4\\ \sqrt{2}(\cos[(2i-9)\pi/4], \sin[(2i-9)\pi/4]), & i = 5-8 \end{cases}$$
(2.10)

 $\Omega = M^{-1}SM$ is the collision matrix, and M is the transformation matrix between the lattice space and velocity space, which is defined as

$$\mathbf{M} = \begin{pmatrix} 1 & 1 & 1 & 1 & 1 & 1 & 1 & 1 & 1 \\ -4 & -1 & -1 & -1 & -1 & 2 & 2 & 2 & 2 & 2 \\ 4 & -2 & -2 & -2 & -2 & 1 & 1 & 1 & 1 \\ 0 & 1 & 0 & -1 & 0 & 1 & -1 & -1 & 1 \\ 0 & -2 & 0 & 2 & 0 & 1 & -1 & -1 & 1 \\ 0 & 0 & 1 & 0 & -1 & 1 & 1 & -1 & -1 \\ 0 & 0 & -2 & 0 & 2 & 1 & 1 & -1 & -1 \\ 0 & 1 & -1 & 1 & -1 & 0 & 0 & 0 & 0 \\ 0 & 0 & 0 & 0 & 0 & 1 & -1 & 1 & -1 \end{pmatrix}$$
 (2.11)

S is a diagonal matrix containing multi-relaxation times in 9×9 dimension [17], and S can be defined as

$$S = diag(0,1.63,1.14,0,1.92,0,1.92,s_v,s_v)$$
 (2.12)

in which $s_{\upsilon} = 0.5 + 1/\tau$ is the relaxation parameter. $\tau = 0.5 + 3\upsilon$ is relaxation time, and $\tau = 0.5 + 3\upsilon$ is the kinematic viscosity.

 $F_i(\mathbf{x},t)$ is the external force term, according to the reference [18], can be calculated by

$$\mathbf{F} = \mathbf{M}^{-1} \left(\mathbf{I} - \frac{1}{2} \mathbf{S} \right) \mathbf{M} \overline{\mathbf{F}}$$
 (2.13)

$$\overline{F}_i = w_i \left[\frac{\boldsymbol{c}_i \cdot \mathbf{G}}{c_s^2} + \frac{\boldsymbol{v} \mathbf{G} : \left(\boldsymbol{c}_i \boldsymbol{c}_i - c_s^2 \boldsymbol{I} \right)}{2c_s^4} \right]$$
(2.14)

in which w_i is the weight factor, and can be defined

as

$$w_i = \begin{cases} 4/9, & i = 0\\ 1/9, & i = 1 - 4\\ 1/36, & i = 5 - 8 \end{cases}$$
 (2.15)

 c_i is the discrete velocity. $c_s^2 = \delta_x^2 / 3\delta_t^2$ is the lattice

sound speed. $\mathbf{G} = G_x \vec{i} + G_y \vec{j}$ represents the resultant external force, including the buoyancy force $G_B(\mathbf{x},t)$, dissipative drag force $G_D(\mathbf{x},t)$ and applied force $G_F(\mathbf{x},t)$, according to the references [19-21], which can be calculated by

$$G(x,t) = G_R(x,t) + G_D(x,t) + G_F(x,t)$$
 (2.16)

$$G_B(\mathbf{x},t) = -\rho \mathbf{g} \beta_c \left(c - c_l^0\right) f_l \tag{2.17}$$

$$G_D(\mathbf{x},t) = -\frac{2\rho vh}{W_0^2} f_l (1 - f_l)^2 v$$
 (2.18)

$$G_{E}(\mathbf{x},t) = -A\rho f_{l}\mathbf{e} \tag{2.19}$$

in which $\rho = \sum_s f_i(x,t)$ is the fluid density in lattice space. $f_l = (1-\phi)/2$ is the fraction of liquid phase. β_c is the solute expansion coefficient. $g = -9.8 \ m/s^2$ is gravitational acceleration. The negative sign indicates the negative direction of *Y*-axis. h = 2.757 is a constant. v is the macroscopic fluid velocity. $A = P_v$ is the acceleration transformed by the external pressure gradient dp/dy, and can be calculated by

$$P_{y} = \frac{dp}{\rho \cdot dy} \tag{2.20}$$

2.3 Simulation condition

To simulate dendritic growth in a space approaching the actual dimensions of thin-walled castings, we selected Al-0.576 wt% Cu alloy as the model alloy due to its larger chemical capillary length. The physical properties and simulation-related parameters for this alloy are presented in Table 1. The time interval in this work is $\Delta t = 0.8 \left(\Delta x\right)^2/\left(4\tilde{D}\right)$. The initial concentration field was set by the dimensionless supersaturation $\Omega_0 = \left(c_l^0 - c\right)/\left(c_l^0\left(1 - k\right)\right) = 0.5$. c_l^0 is the initial concentration of liquid phase at the solid-liquid phase interphase.

The boundary conditions for all simulations are illustrated in Fig.1. For phase-field and concentration field, the top and bottom boundaries are set as periodic boundary conditions. The left boundary uses a zero-flux boundary condition, while the right boundary is a symmetric boundary condition. For flow field, the top and bottom boundaries are again periodic boundary conditions. The left boundary employs non-equilibrium extrapolation scheme for non-slip boundary conditions. The right boundary is set as symmetric. Finally, the boundaries between the fluid and solid dendrites are defined by no-slip boundary conditions with a bounce-back scheme.

Tab. 1 The physical properties of Al-0.576 wt% Cu

Parameter	Symbol	Value
Nominal concentration (wt%)	\mathcal{C}_{∞}	0.576
Liquidus slope (K/wt%)	m	-2.7[22]
Equilibrium solute partition coefficient	k	0.14[23]
Solute diffusion coefficient in liquid ($\mu m^2/s$)	D	3000[23]
Solute expansion coefficient (1/wt%)	eta_c	-0.73[12]
Gibbs-Thomson coefficient (K·μm)	Γ	0.24[23]
Kinematic viscosity (m ² /s)	v	4.851×10 ⁻⁷
Interface width (µm)	W_0	0.9375[23]
Gravitational acceleration (m/s²)	g0	-9.8
Cooling speed (K/s)	R	1
Temperature gradient (K/mm)	G	2
Transformed acceleration (m/s ²)	P_y	0.01
Anisotropic strength	€4	0.02
Space interval (W0)	Δx	0.8

In this work, for isothermal solidification of equiaxed dendrites, the simulation domain is $1000\Delta x \times 1000\Delta y$ ($\Delta y = \Delta x$) = 0.75×0.75 mm². For directional growth of dendrites, the simulation domain is $1000\Delta x \times 1200\Delta y$ ($\Delta y = \Delta x$) = 0.75×0.9 mm². This study employs a hybrid programming approach utilizing Python and Taichi language to leverage Graphics Processing Unit (GPU) acceleration for simulations. All simulations were conducted on a single NVIDIA Tesla V100-SXM2 GPU.

3 Results and discussion

3.1 Effects of convection on the equiaxed dendritic morphologies

As shown in Fig. 2, the solidification morphologies evolution of equiaxed dendrites under natural convection and forced convection has been investigated. Under no convection condition (Figs. 2(a1) and (a2)), the lengths of four primary dendritic trunks are comparable. However, when natural convection was present (Figs. 2(b1) and (b2)), the upstream dendrites grew faster than those downstream ones, and the secondary dendrites appeared on the upstream primary dendrite trunks. The growth of downstream dendrites was suppressed and existed splitting phenomenon, resulting from an accumulation of solute. For β_c <0, the rejected solute accumulated

downstream under gravity, leading to the solute plume phenomenon (Fig. 2(b1)), which is closely relative to the formation of freckle in castings [24]. Here, when g = -g0 (Figs. 2(c1) and (c2)), because of buoyancy force, the solute plume appeared at the upper side. When the $P_y = 0.01$ m/s² was present (Figs. 2(d1) and (d2)), at t = 0.375 s, the length of downstream primary dendrite is larger than that of upstream primary dendrite, which indicated that there was a reversal of flow direction. The effects of natural convection caused by gravity were decreased, leading to the central position of solute plume being closer to the dendrite tip.

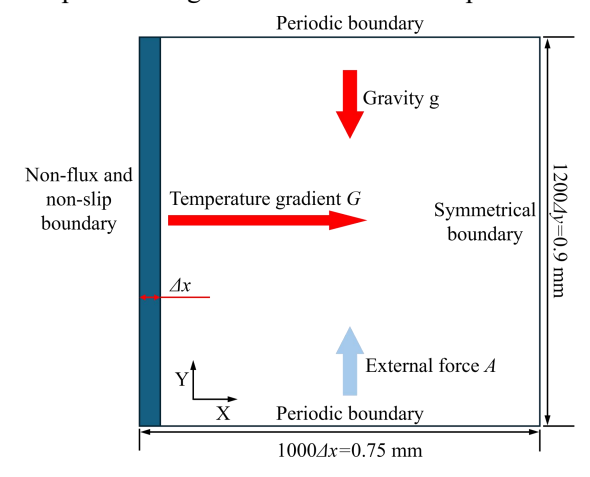
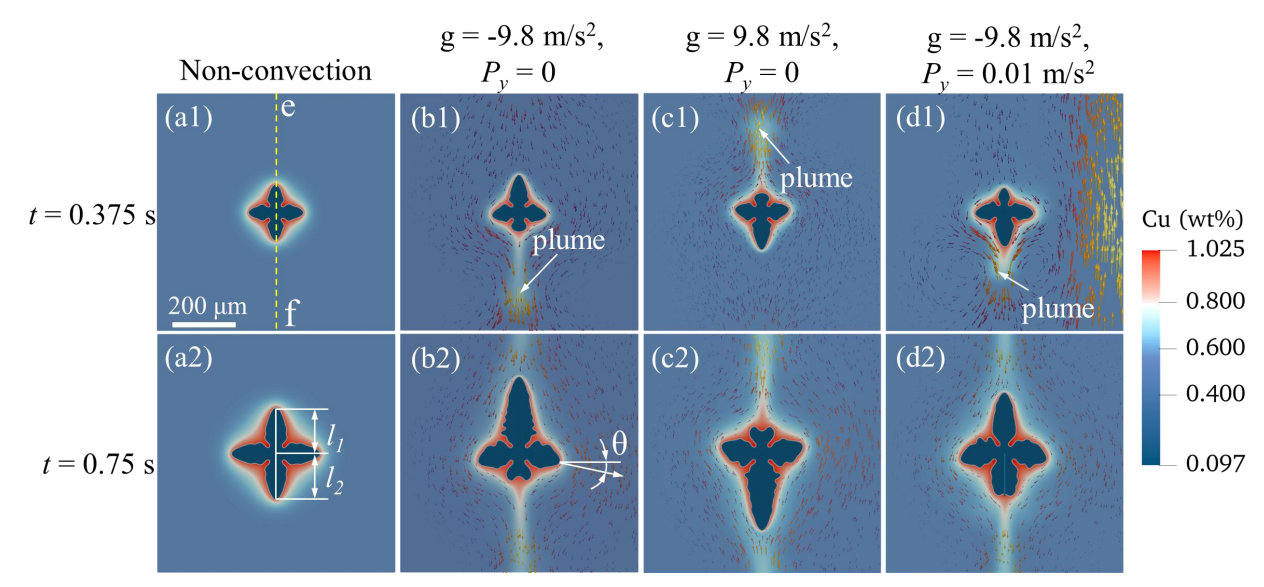


Fig. 1 Simulation conditions for directional dendritic growth.



To further study the relation between the dendrite morphologies and convections, as shown in Fig. 3, the concentration along e-f line (seen in Fig. 2(a1)) was investigated. Under convections, the maximum concentration values around the upstream dendrite tip were 0.954 wt% ($P_y = 0$), and 0.942 wt% ($P_y = 0.01$

m/s²), which are larger than 0.878 wt% of that without convection. Meanwhile, when $P_v = 0.01$ m/s², the maximum concentration around the downstream dendrite tip was 0.834 wt%, higher than that when P_{ν} = 0. The high solute concentration around dendrite tips can decrease the local melting point, leading to the decrease of local undercooling. Therefore, the growth velocity of dendrite tip decreases. Consequently, the length of the downstream dendrite trunk can be shorter than that of the upstream dendrite trunk, and the horizontal primary dendrite trunks deflect (seen in Fig. 2(b2)) [12]. The deflection angle was measured by ImageJ. Under convections, when $P_v = 0$, the deflection angle θ was 17.556°, while θ was 15.48° when $P_y =$ 0.01 m/s². The deflection angle decreased 2.076°, resulting from the decrease of convection strength

around the dendrite. An asymmetry degree δ was used to quantitively analyze the length difference between the upstream primary dendrite trunk and downstream primary dendrite trunk. δ is defined as:

$$\delta = \frac{|l_1 - l_2|}{l_1 + l_2} \tag{3.1}$$

in which l_1 and l_2 are the lengths of the upstream primary dendrite trunk and downstream primary dendrite trunk, respectively (seen in Fig. 2(a2)). When t=0.75 s, under no convection, $\delta=0$, while $\delta=0.52$ when $P_y=0$, and $\delta=0.17$ when $P_y=0.01 \text{m/s}^2$ under convections. Therefore, within an appropriate applied force in casting, the dendrite morphologies can be more symmetrical.

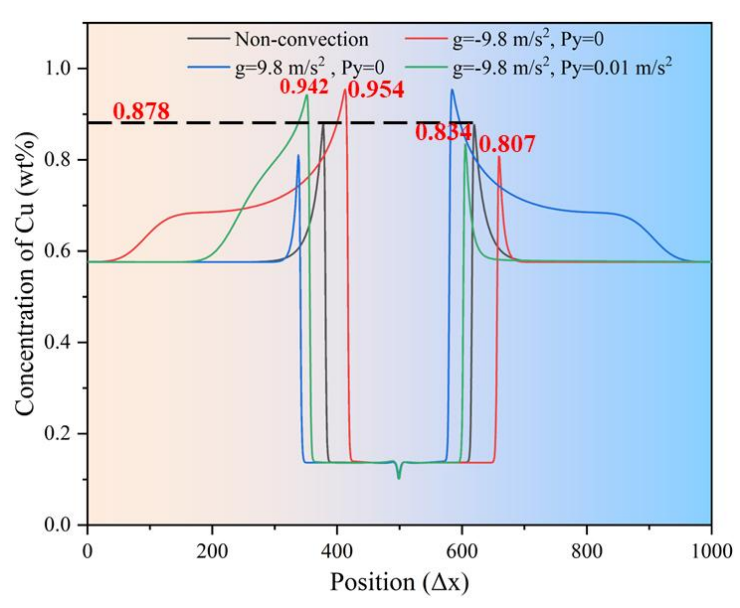


Fig. 3 The concentration distribution of solute Cu along line e-f under different convections

3.2 Effects of convection on the directionally solidified dendritic morphologies

In thin-walled casting molds, nucleation typically initiates at the colder side walls, followed by dendritic growth progressing toward the central region [11]. Therefore, as shown in Fig. 4, the directional dendritic growth has been simulated. Under convections, the growth direction of the dendrites becomes inclined toward the direction of fluid flow. When $P_y = 0$ (Fig. 4(b)), the deflection angle of the dendrites was 5.32° . When $P_y = 0.01 \text{m/s}^2$ (Figs. 4(c) and (d)), the deflection angle of the dendrites was 4.45° , which decreased 0.87° ,

resulting from the decrease of convection strength around the dendrite tips. Interestingly, there was a transformation of convection modes. As shown in Fig. 4(c), at t = 1.5 s, natural convection induced by gravity dominated near the dendrite tips, resulting in a fluid velocity primarily oriented along the negative *Y*-axis. However, in the region farther from the dendrites, where solute enrichment was relatively weak, the convection was mainly driven by the forced convection caused by the applied force. As the dendrites grew, the solute concentration in the distal region gradually increased. By t = 2.25 s, natural convection became dominant throughout the thin-walled

domain, and the overall fluid motion aligns with the

negative Y-direction.

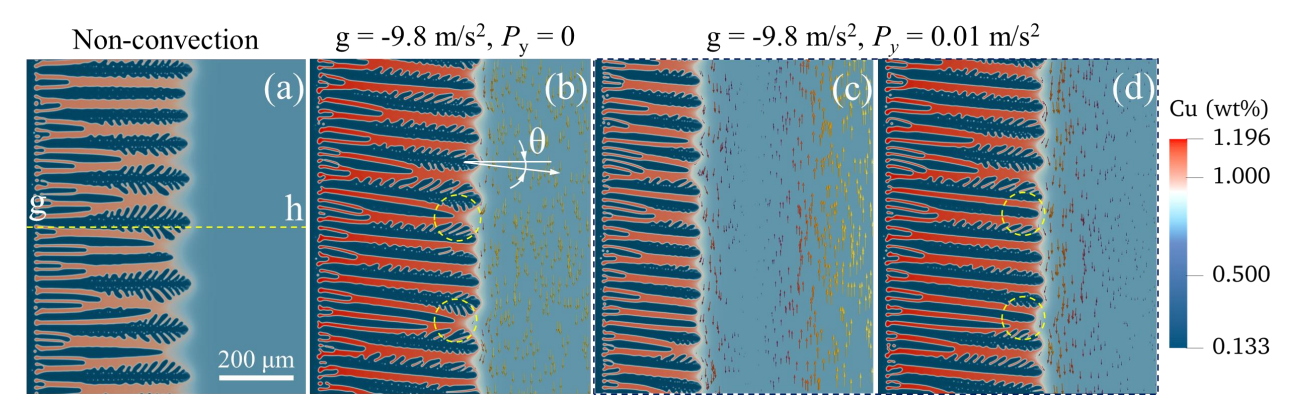


Fig. 4 Simulation results of directional dendrites growth under different convections: (a) non-convection, (b) g = g0 and $P_y = 0$, (c)-(d) g = g0 and $P_y = 0.01$ m/s². (c) is at t = 1.5 s; (a), (b) and (d) are at t = 2.25 s.

As shown in Figs. 4(b) and 4(d), when $P_y = 0.01$ m/s², the development of secondary dendrites is suppressed, the competition between primary and secondary dendrites is alleviated (see the yellow dashed circles in Figures 4(b) and 4(d)). As a result, the primary dendrites gained a growth advantage. Consequently, the solidification microstructure was finer than that when $P_y = 0$.

By analyzing the melt velocity along the g-h line (Fig. 4(a)), the convection behavior ahead of the dendrite tips can be evaluated. As illustrated in Fig. 5, when $P_y = 0.01$ m/s², with the continued growth of dendrites, the fluid velocity in the distal region along the *Y*-axis eventually shifts fully in the negative *Y*-direction, indicating that gravity-driven natural convection becomes the prevailing flow mechanism. The flow velocity (-0.0013 m/s) around the dendrite tips is lower than that (-0.0017 m/s) when $P_y = 0$, indicating the decrease of convection strength.

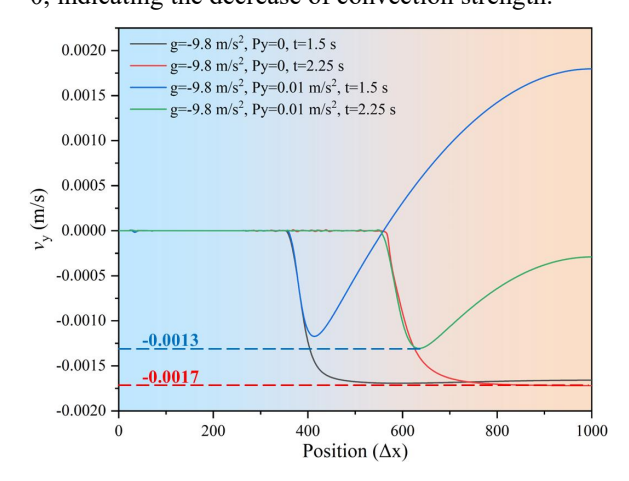


Fig. 5 The velocity distribution along line g-h in the Y-direction under different convections

4 Conclusions

This study coupled the multiple-relaxation-time Lattice Boltzmann method with the binary Karma phase-field model to simulate the influence of different convection conditions on the morphology of Al-0.576 wt% Cu equiaxed grains and directionally solidified columnar dendrites within thin-walled spaces. The main conclusions are as follows:

- (1) Equiaxed grains exhibited solute plume phenomena under gravity-driven natural convection, leading to significant differences in the development of upstream and downstream dendrites. When $P_y = 0.01 \text{ m/s}^2$ was present, the intensity of gravity-induced convection was reduced. The distance between the solute plume center and the dendrite tip decreased, and the tilt angle of the primary dendrite arms growing on the left and right sides was reduced from 17.556° to 15.48°.
- (2) Under conditions of the temperature gradient G = 2 K/mm and the cooling rate R = 1 K/s, convection caused directionally solidified dendrites within the thin-walled space to tilt in the direction of fluid motion. This tilt angle decreased with a reduction in the overall convection intensity. When $P_y = 0.01$ m/s² was present at time t = 1.5 s, convection near the dendrite tips in the thin-walled space was predominantly gravity-induced natural convection, while forced convection due to P_y dominated at the far end. As the dendrites grew within the thin-walled space, the overall convection form became primarily natural convection.
 - (3) By simulating the growth morphology of equiaxed

grains and directionally solidified dendrites under various convection conditions in thin-walled spaces, this research further elucidates the microscopic solidification mechanisms in both gravity casting and counter-gravity casting of thin-walled components. This provides valuable theoretical guidance for actual production practices.

Acknowledgments

This work was financially supported by the Advanced Materials-National Science and Technology Major Project (No. 2024ZD0600400), the Aeronautical Science Fund of China (No. 2023Z053057003), the Science and Technology Commission of Shanghai Municipality, China (No. 23ZR1428800).

Conflicts of interest:

The authors declare that they have no known competing financial interests or personal relationships that could have appeared to influence the work reported in this paper.

References

- [1] YU Z.W, LI F.G, ZHANG J, DONG A.P, SUN B.D, Progess of the counter gravity casting technology in the superalloy large complicated thin-walled castings (in Chinese), J. Spec. Cast. & Nonferr. Alloy., 32(12) (2012) 1103-1106.
- [2] FENG Z.J, LI Y.F, WANG W, SHI F, WU J, RUAN M, Counter-gravity casting (in Chinese), Found. Equip. Technol. (2019) 71-76.
- [3] HUANG J.M, ZHAO H.D, CHEN Z.M. Microstructure and Properties of A356 Alloy Wheels Fabricated by Low-Pressure Die Casting with Local Squeeze[J]. Journal of Mater. Eng. Perform., 2019, 28:2137-2146.
- [4] DONG G, LI S, MA S, et al. Process optimization of A356 aluminum alloy wheel hub fabricated by low-pressure die casting with simulation and experimental coupling methods[J]. J. Mater. Res. Technol., 2023, 24:3118-3132.
- [5] LEHMHUS D, CEN M, STRUSS A, et al. Thick Film Sensor Manufacturing Techniques for Realization of Smart Components via Low Pressure Die Casting[J]. J. Phys: Confer. Ser., 2024, 2692:012007.
- [6] HUANG X, XUE X, WANG M, et al. Hot Tearing Behavior of ZL205A Alloy Cylindrical Low-Pressure Castings with

- Slit Gating and Feeding System[J]. Int. J. Metalcast., 2023, 17:2970-2980.
- [7] JARFORS A.E.W., Pressure Different Casting, Encyclopedia of Materials: Metals and Alloys, 2022, pp. 117-128.
- [8] LIU S.G, CAO F.Y, YI J.Y, et al. Effect of depressurizing speed on mold filling behavior and entrainment of oxide film in vacuum suction casting of A356 alloy[J]. T. Nonferr. Metal. Soc., 2016, 26:3292-3298.
- [9] DONG A.P, DU. D.F, XING H., ZHU, G.L, Advanced Adjusted Pressure Casting Process, Precision Forming Technology of Large Superalloy Castings for Aircraft Engines, Springer Singapore, Singapore, 2021, pp. 355-406.
- [10] YAN Q.S, YU H, XU Z.F, XIONG B.W, CAI C.C, Effect of holding pressure on the microstructure of vacuum counter-pressure casting aluminum alloy, J. Alloy. Compd., 501(2) (2010) 352-357.
- [11] LI F, ZHANG J, BIAN F, et al. Mechanism of Filling and Feeding of Thin-Walled Structures during Gravity Casting[J]. Materials, 2015, 8:3701-3713.
- [12] ZHANG A, MENG S, GUO Z, et al. Dendritic Growth Under Natural and Forced Convection in Al-Cu Alloys: From Equiaxed to Columnar Dendrites and from 2D to 3D Phase-Field Simulations[J]. Metall. Mater. Trans. B, 2019, 50:1514-1526.
- [13] ZHANG Y.J, ZHOU J.X, YIN Y.J, SHEN X, JIX.Y, LI W, Numerical Simulation of Dendrite Growth and Solute Convection during Directional Solidification of Superalloy [J]. J. Netshape. Form. Eng., 2023, 15(10): 13-20.
- [14] ECHEBARRIA B, FOLCH R, KARMA A, et al. Quantitative phase-field model of alloy solidification[J]. Phys. Rev. E, 2004, 70:061604.
- [15] KARMA A. Phase-field formulation for quantitative modeling of alloy solidification[J]. Phys. Rev. Lett., 2001, 87:115701.
- [16] WU J, SUN D, CHEN W, et al. A unified lattice Boltzmann phase field scheme for simulations of solutal dendrite growth in the presence of melt convection[J]. Int. J. Heat Mass Transfer, 2024, 220.
- [17] LALLEMAND P, LUO L.S. Theory of the Lattice Boltzmann Method: Dispersion, Dissipation, Isotropy, Galilean Invariance, and Stability[J]. Phys. Rev. E, 2000, 61:6546-6562.
- [18] GUO Z, ZHENG C. Analysis of lattice Boltzmann equation for microscale gas flows: Relaxation times, boundary



- conditions and the Knudsen layer[J]. Int. J. Comput. Fluid D, 2008, 22:465-473.
- [19] YANG C, XU Q, LIU B. Study of dendrite growth with natural convection in superalloy directional solidification via a multiphase-field-lattice Boltzmann model[J]. Comp. Mater. Sci., 2019, 158:130-139.
- [20] ZHANG Y, ZHOU J, YIN Y, et al. Study on the solutal convection during dendrite growth of superalloy under directional solidification condition[J]. J. Mater. Res. Technol., 2023, 23:3916-3927.
- [21] ZHANG A, DU J, GUO Z, et al. A Phase-Field Lattice-Boltzmann Study on Dendritic Growth of Al-Cu Alloy Under Convection[J]. Metall. Mater. Trans. B, 2018,

- 49:3603-3615.
- [22] BOUKELLAL A K, ROUBY M and DEBIERRE J M. Tip dynamics for equiaxed Al-Cu dendrites in thin samples: Phase-field study of thermodynamic effects[J]. Comp. Mater. Sci., 2021, 186:110051.
- [23] TAKAKI T, OHNO M, SHIMOKAWABE T, et al. Two-dimensional phase-field simulations of dendrite competitive growth during the directional solidification of a binary alloy bicrystal[J]. Acta Mater., 2014, 81:272-283.
- [24] REN N, LI J, Panwisawas C, XIA M.X, DONG H.B, LI J.G, Insight into the sensitivities of freckles in the directional solidification of single-crystal turbine blades, J. Manuf. Process. 77 (2022) 219-228.